micromachines

MDPI

Article

Polarization Engineered p-Type Electron Blocking Layer Free AlGaN Based UV-LED Using Quantum Barriers with Heart-Shaped Graded Al Composition for Enhanced Luminescence

Samadrita Das [1], Trupti Ranjan Lenka [1,*], Fazal Ahmed Talukdar [1], Hieu Pham Trung Nguyen [2] and Giovanni Crupi [3]

[1] Department of Electronics and Communication Engineering, National Institute of Technology Silchar, Silchar 788010, Assam, India; samadrita_rs@ece.nits.ac.in (S.D.); fazal@ece.nits.ac.in (F.A.T.)
[2] Department of Electrical and Computer Engineering, Texas Tech University, 1012 Boston Avenue, Lubbock, TX 79409, USA; hieu.p.nguyen@ttu.edu
[3] BIOMORF Department, University of Messina, 98125 Messina, Italy; giovanni.crupi78@unime.it
* Correspondence: trlenka@ieee.org

Abstract: In this paper, in order to address the problem of electron leakage in AlGaN ultra-violet light-emitting diodes, we have proposed an electron-blocking free layer AlGaN ultra-violet (UV) light-emitting diode (LED) using polarization-engineered heart-shaped AlGaN quantum barriers (QB) instead of conventional barriers. This novel structure has decreased the downward band bending at the interconnection between the consecutive quantum barriers and also flattened the electrostatic field. The parameters used during simulation are extracted from the referred experimental data of conventional UV LED. Using the Silvaco Atlas TCAD tool; version 8.18.1.R, we have compared and optimized the optical as well as electrical characteristics of three varying LED structures. Enhancements in electroluminescence at 275 nm (52.7%), optical output power (50.4%), and efficiency (61.3%) are recorded for an EBL-free AlGaN UV LED with heart-shaped Al composition in the barriers. These improvements are attributed to the minimized non-radiative recombination on the surfaces, due to the progressively increasing effective conduction band barrier height, which subsequently enhances the carrier confinement. Hence, the proposed EBL-free AlGaN LED is the potential solution to enhance optical power and produce highly efficient UV emitters.

Keywords: GaN; AlGaN; AlInN; ultra-violet (UV); electron blocking layer (EBL); light-emitting diode (LED); multi-quantum well (MQW)

Citation: Das, S.; Lenka, T.R.; Talukdar, F.A.; Nguyen, H.P.T.; Crupi, G. Polarization Engineered p-Type EBL Free AlGaN Based UV-LED Using Quantum Barriers with Heart-Shaped Graded Al Composition for Enhanced Luminescence. *Micromachines* **2023**, *14*, 1926. https://doi.org/10.3390/mi14101926

Academic Editors: Julien Brault, Hao-Chung Kuo, Hsin-Chu Chen and Yi-Jen Chiu

Received: 26 August 2023
Revised: 3 October 2023
Accepted: 12 October 2023
Published: 13 October 2023

1. Introduction

Due to the direct tunable band gap, between 3.43 eV and 6.11 eV, AlGaN ternary alloy is quite applicable to the fabrication of optical devices within a wavelength range of ~200–360 nm [1]. This is suitable for sterilization [2–5], ultra-violet printing [6,7], biomedical appliances [8,9], deodorization using a photo catalyst [10,11], dermatology in medicine [12,13], and sensing applications for materials, for example urea [14,15]. However, the internal quantum efficiency (IQE) and light output power (LOP) of UV-LEDs using AlGaN alloys are still low because of several adversities. Due to the overflow of electrons at high currents, the problem of efficiency drop occurs [16]. This happens because strong induced polarization fields and quantum-confined Stark effect (QCSE) [17] lead to a significant separation of electron and hole wave functions. Thus, there is a reduction of carrier confinement and radiative recombination in the quantum well of the

device.

To a certain extent, the overflow of electrons is eliminated by bringing a p-doped Al-rich electron blocking layer (EBL) between the multi-quantum well (MQW) and p-doped area [18]. However, the development of positively charged polarization sheet charges within the hetero-interface of the ultimate quantum barrier (QB) and EBL has a significant impact on the hole effectiveness [19,20]. Additionally, due to Al abundant EBL, magnesium doping efficiency is also impacted by high acceptor activation energy [21,22]. To mitigate the aforesaid challenges, various LED structures with re-designed EBL and QW have been addressed [23–27]. However, only a few challenges were able to be reduced, hence it is favorable to create EBL-free UV-LEDs resulting in an enhanced flow of carriers.

To tackle the difficulties caused by EBL, in this paper an EBL-free UV-LED with heart-shaped QBs has been presented operating at ~275 nm wavelength. The conventional AlGaN UV-LED consists of a thin intrinsic AlGaN strip placed into the center of each QB. In our context, this design is modified with the utilization of heart-shaped QBs on the first five barriers. The heart-shaped graded Al composition-based UV LED shows the highest quantum efficiency and reduced efficiency drop due to the reduced polarization field and the elimination of the EBL layer in the device structure resulting from the progressively graded QBs. This unique LED structure offers a significantly reduced electrostatic field in the quantum well (QW) region due to the decreased lattice mismatch between the QW and the QB. Furthermore, the internal quantum efficiency of the proposed LED exhibits a massive enhancement due to the increased carrier confinement in the device active region and the reduced electron leakage to the p-type region resulted from the progressive increase in the effective conduction band barrier heights. Moreover, the hole injection efficiency of the proposed LED structures is greatly increased due to the reduced positive polarization sheet charges at the interface of the last QB and EBL, achieved later from the EBL. Consequently, the output power and wall-plug efficiency (WPE) of the proposed LED structure show significant enhancements compared to the conventional LEDs which are about 50.4% and 49.3%, respectively.

2. Structural Parameters

In this study, the performance of three distinct AlGaN-based UV LED devices with non-identical MQWs and EBLs has been evaluated. To carry out the simulation, the ABC-model is used as the physical model for underlying the calculations. This model is based on the following assumptions: (i) carrier leakage from an LED structure's active region does not result in carrier losses, (ii) active region's non-equilibrium electron (n) and hole (p) concentrations are almost identical to one another, and (iii) carrier concentrations have a negligible impact on the recombination coefficients A, B, and C (details are explained below).

The deep ultra-violet LED fabricated by Yan et al. [28] is considered as the conventional device for reference (LED_1) as shown in Figure 1a. The device has a dimension of 400×400 μm^2 with ~275 nm wavelength emission. An AlN buffer layer and 3 μm-widen-AlGaN (60% Al; Si: 5×10^{18} cm^{-3}) layers are settled over the substrate. The following active region comprises of 5 periods of 10 nm thick intrinsic AlGaN (50% Al) QBs and 3-nm-thick AlGaN (40% Al) quantum wells (QWs), 20 nm thick p-$Al_{0.65}Ga_{0.35}N$ EBL (Mg: 2×10^{19} cm^{-3}), succeeded by a 50 nm p-AlGaN (50% Al) cladding layer (Mg: 2×10^{19} cm^{-3}), and finally a p-GaN contact layer of 120 nm width (Mg: 1×10^{20} cm^{-3}). The Al composition (%) profile in the active region and EBL related to the conduction band energy diagram of LED_1 is presented in Figure 1b.

As illustrated from the conduction band energy diagram in Figure 1c, LED_2 is constructed from LED_1 by replacing the uniform composition AlGaN EBL with an $Al_xIn_{1-x}N$ layer which has a graded Al composition (x: 0.65–0.35). LED_2 includes a 3.5 nm $Al_{0.6}Ga_{0.4}N$ single spike barrier and an 8.5 nm thick $Al_{0.5}Ga_{0.5}N$ barrier in spite of the undoped AlGaN barriers; excluding the first barrier which is nearest to the n-doped area.

The proposed device (LED_3) in Figure 1d is finally realized by discarding the EBL and introducing graded Al composition to each of the heart-shaped barriers, with the exception of the first one. The remaining 10 nm intrinsic QBs are now composed of graded Al (x: 0.45–0.5–0.45–0.5–0.45) to form the heart-shaped structure.

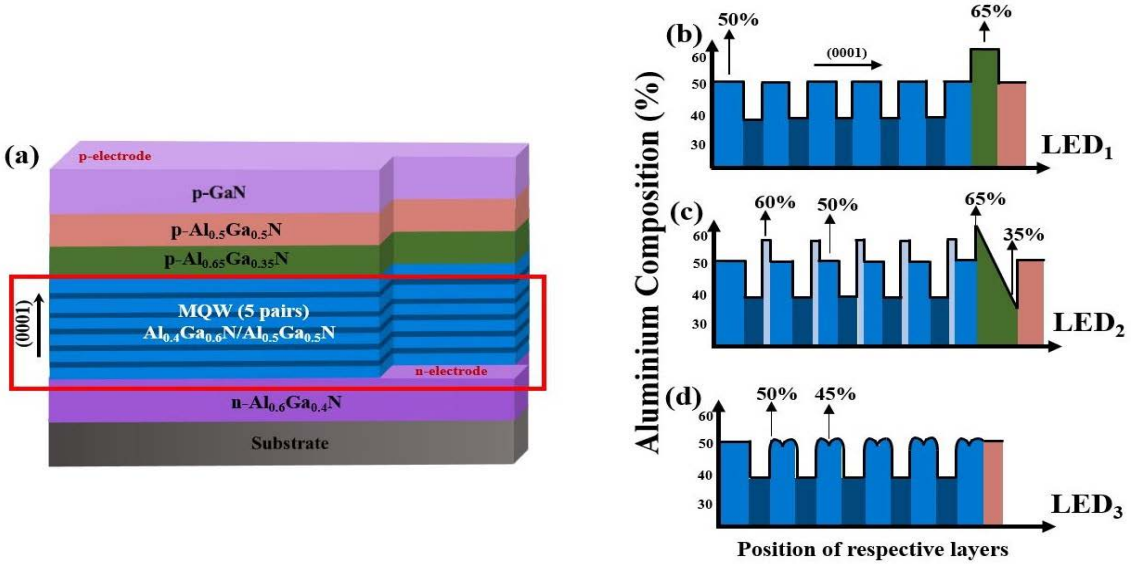

Figure 1. (**a**) Schematic diagrams of LED_1, Aluminum composition (%) related to the conduction band of (**b**) LED_1, (**c**) LED_2, and (**d**) LED_3.

The electrical and optical characteristics of the device architectures are precisely recreated in this numerical analysis and studied with the help of commercially available industry-standard Silvaco ATLAS technology computer-aided design (TCAD).

In our work, we have used the Varshni formula to estimate the energy band gap of AlGaN as follows [29]:

$$E_g(T) = E_g(0) - \frac{\alpha T^2}{\beta + T} \quad (1)$$

where α and β represent material constants, $E_g(0)$ and $E_g(T)$ denote the energy band-gap at 0, and T represents temperature, whose values are listed in Table 1 [30]. Equation (2) can be used to compute the band gap energy of $Al_xGa_{1-x}N$ using these values, as shown below [31]:

$$E(Al_xGa_{1-x}N) = x.E^{AlN} + (1-x).E^{GaN} - b.x.(1-x) \quad (2)$$

where b = 0.94 is the bowing parameter, band-offset ratio is taken as 0.68/0.35 [31]. Constructing the band gap energy or band structures of the LEDs is an important step to understand the carrier transport, electron leakage, recombination mechanism, and electrostatic fields, which are explained in the following figures. These parameters are helpful in elucidating the performance of the devices, including quantum efficiency, wall-plug efficiency, and optical and electrical properties, which are presented and explained further.

Table 1. Respective values of material constants for GaN, AlN [29].

Materials	α	β	$E_g(0)$
GaN	0.919 meV/K	820 K	3.507 eV
AlN	1.789 meV/K	1432 K	6.23 eV

The energy band diagrams and carrier mobility are calculated using a 6 × 6 k.p model [32] and the Caughey–Thomas approximation [33], respectively. The Shockley-Read-Hall (SRH), Radiative, and Auger recombination co-efficients are taken as 6.67 × 10^7/s, 2.13 × 10^{-11} cm^3/s and 2.88 × 10^{-30} cm^6/s, respectively [34,35], and the SRH recombination lifetime is set to 15 ns. The light extraction efficiency is considered to be 15%. Moreover, the Mg activation energy varies across 165 meV to 515 meV for p-$Al_xGa_{1-x}N$ alloy [22]. From the methods of Fiorentini et al., the built-in polarization (spontaneous as well as piezoelectric) is estimated [36]. The entire simulation was carried out at a temperature of 300 K. The electron and hole mobilities are set to be 100 $cm^2V^{-1}s^{-1}$ and 5 $cm^2V^{-1}s^{-1}$ and other band parameters are available elsewhere [37].

3. Results and Discussion

With the use of experimentally obtained data from standard LED_1, the device model, parameters, and tools employed in this work were optimized. The numerical simulation of the power-current-voltage graphs of LED_1 in Figure 2 closely matches the practically obtained curves, demonstrating the accuracy and dependability of our proposed design.

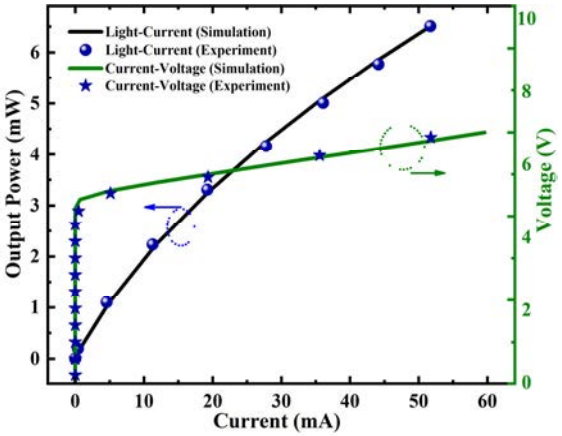

Figure 2. Measured and calculated light-current-voltage characteristics of LED_1 for model validation.

Then, numerical simulations on the electrical and optical properties of LED_1, LED_2, and LED_3 were carried out and the outcomes were compared one after another. Figure 3 illustrates the energy band diagrams (green solid lines) and quasi-Fermi levels (red dotted lines) of the three device samples at a 60 mA injected current. The variation in energy across the conduction/valence band and the quasi-Fermi levels is used to establish the efficient potential barrier heights for particles in the EBL (ϕ_E) and QBs (ϕ_{CN}). The optimum potential barrier height is acknowledged as the crucial factor in figuring out how to move the carrier. The corresponding values of ϕ_{CN} and ϕ_E are estimated from Figure 3a–c and listed in Table 2.

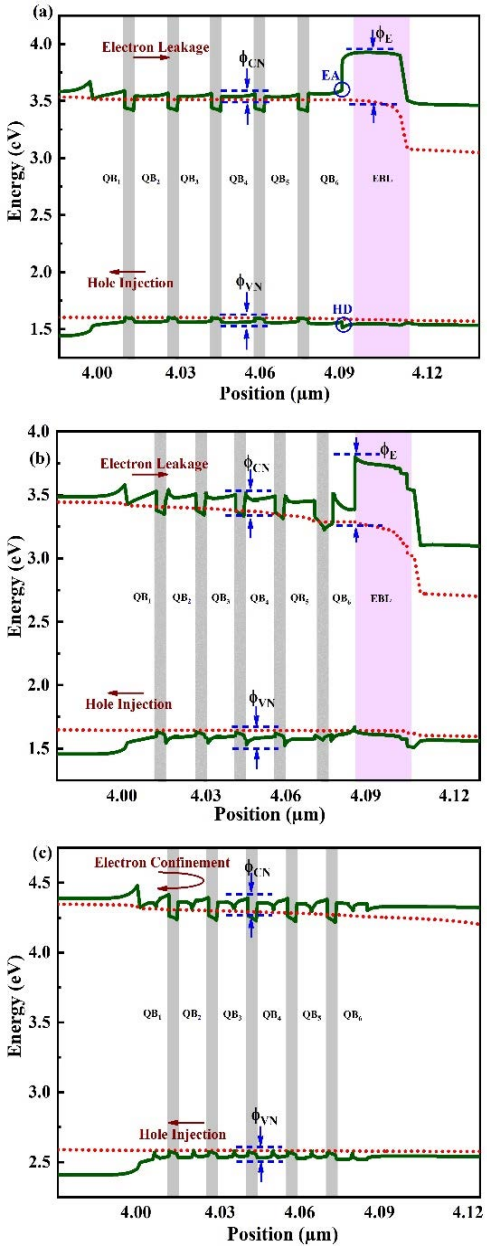

Figure 3. Estimated energy-band diagrams of (**a**) LED_1, (**b**) LED_2, and (**c**) LED_3 at an injection current of 60 mA. E.A and H.D are the electron accumulation region in the conduction band and hole depletion region in the valence band, respectively.

Table 2. Effective CBBH of barriers (ϕ_{CN}) and EBL (ϕ_E) for LED_1, LED_2, and LED_3.

CBBH (meV)	LED_1	LED_2	LED_3
ϕ_{C1}	145.8	102.3	102.1
ϕ_{C2}	164.4	110.7	109.1
ϕ_{C3}	231.2	112.7	129.3
ϕ_{C4}	298.1	115.9	194.0
ϕ_{C5}	327.6	117.2	215.3
ϕ_{C6}	249.8	121.4	311.9
ϕ_E	244.1	256.0	

Hole injection efficiency in LED_1 is reduced by the hole depletion zone that forms as a result of polarization charge sheet contact across EBL/LQB. The ϕ_E to prevent the excess of electrons in LED_1 is 244.1 meV, which is relatively low compared to the ϕ_E and last QB height (ϕ_{C6}) of LED_2 and LED_3. Due to the AlGaN spikes in the first five barriers of LED_2, a critical polarization field is generated due to high mismatch of lattices which reduces the CBBH and could possibly escalate the electron leakage. Nevertheless, in LED_3, the heart-shaped graded QB results are in better match of the lattice. As a result, the polarization field has dropped and remarkably raised the CBBH, thus putting forward that the final LED design can prevent electron leakage to a great extent. Also, LED_3 shows a progressive growth in ϕ_{CN} values while gradually increasing the amount of aluminum in the QBs. As a result, the electrons are resisted from jumping out of the wells and are confined within. Therefore, the hole injection into the active region increases while non-radiative recombination in the p-region decreases. The integration of heart-shaped graded Al composition in the middle of each QB supports the idea that the negative polarization sheet charges cause the creation of regions that are being accumulated by holes. Since LED_3 has the maximum CBBH, or ϕ_{C6}, it is clear that LED_3 is the best option for containing electrons in the active zone. But a stronger electric field is produced in the active region of LED_2, due to an extremely large lattice imbalance within the QBs and QWs, which has an impact on carrier containment. Moreover, Table 3 calculates and provides a list of the effective VBBH ϕ_{VN} due to each QB. In comparison to LED_1, LED_2, and LED_3 have higher values of ϕ_{VN}, which rises with the graded Al content of the QBs. This bolsters the enhanced hole concentration and better hole containment in the active region.

Table 3. Effective VBBH of barriers (ϕ_{VN}) for LED_1, LED_2, and LED_3.

VBBH (meV)	LED_1	LED_2	LED_3
Φ_{V1}	225.2	302.3	252.1
Φ_{V2}	224.7	317.1	261.7
Φ_{V3}	223.1	329.0	272.4
Φ_{V4}	222.2	362.3	289.6
Φ_{V5}	221.9	372.1	294.2
Φ_{V6}	220.3	384.6	309.5

Figure 4 show the three LEDs' carrier concentration, leak of electrons, and radiative recombination rate at 60 mA injection current. According to our analysis of Figure 4a, LED_1 shows a crucial electronic accumulation near the LQB/EBL junction and a significantly lower electronic concentration in the MQW. Additionally, all the QWs had a greater electron concentration due to LED_3's noticeably higher CBBH. According to Figure 4b, LED_3 had a higher concentration of holes in the QWs. This shows that both hole transfer and hole injecting efficiency have been improved as a result of the decreased VBBH in LED_3.

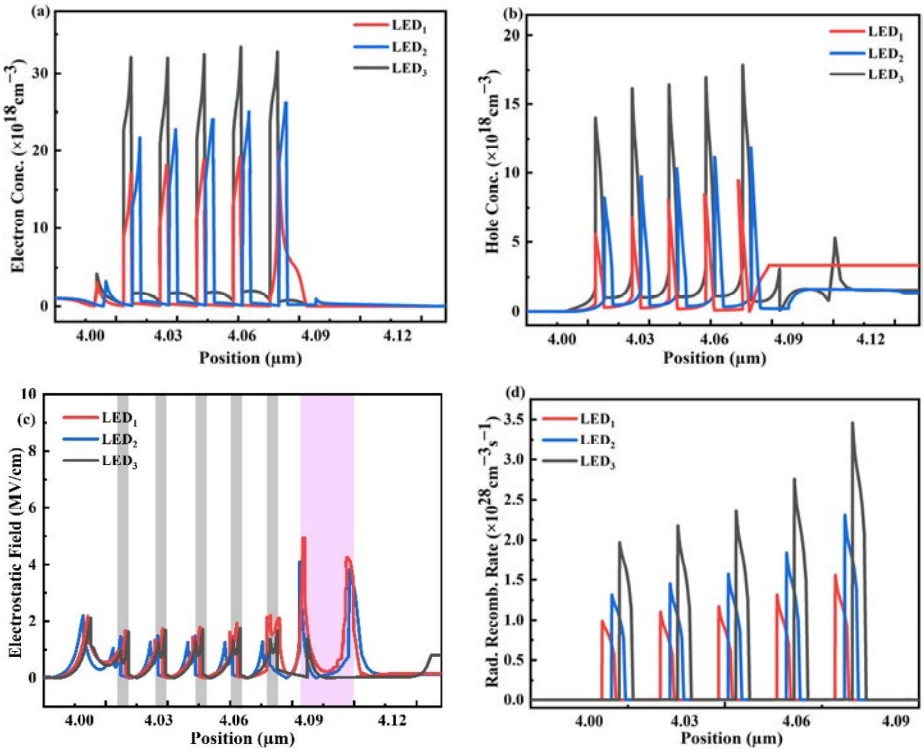

Figure 4. Calculated (**a**) electron concentration, (**b**) hole concentration, (**c**) electrostatic field in the active region, and (**d**) radiative rate of recombination of three structures.

There is a strong electron accumulation in the well and barrier regions and minimal negative electrostatic field in LED_3, because of which electron leakage is tremendously suppressed in the p-region, as shown in Figure 4c. The gray lines represent the QWs while the pink area signifies the EBL for LED_1 and LED_2. With less chance of non-radiative combination of incoming holes with overflowing electrons, hole injection efficiency is increased. Also, as LED_2 has larger electron leakage, so the non-radiative recombination increases and the hole injection efficiency decreases.

The radiative recombination in all the QWs of LED_3 is higher, as displayed in Figure 4d, because of better overlap of the carrier wave functions [38], minimization of electron leakage, and betterment in hole efficiency [39].

In order to have a better understanding of the physical mechanism of enhanced electron confinement in our final device LED_3, the electrostatic field in the active region is studied mathematically. The same can be estimated using the equations marked as (3)–(5) [40].

$$E_{QB} \approx \frac{t_{QW} \times \Delta P(w)}{t_{QW} \times \varepsilon_{QB} + t_{QB} \times \varepsilon_{QW}} \tag{3}$$

$$E_{QB} \times t_{QB} = E_{QW} \times t_{QW} \tag{4}$$

$$\Delta P(w) = \sigma_{interface} - \rho_{QB} \times w \tag{5}$$

E_{QB} and E_{QW} are the electrostatic fields in QB and QW, respectively. $\Delta P(w)$ denotes net polarization charge density along the growth direction 'w'. ε_{QB} and ε_{QW} represent dielectric constants of the barrier and well, respectively, and their respective widths are t_{QW} and t_{QB}. Because of the poor electrostatic field in the well, the electrons and holes are confined effectively [25]. Equation (4) depicts that E_{QB} and E_{QW} are directly proportional to each other. Also, from Equation (3), E_{QB} can be minimized by decreasing the

values of $\Delta P(w)$ which is eventually connected to $\sigma_{interface}$ and ρ_{QB}, as given in Equation (5). Again, using the following equations, the values of $\sigma_{interface}$ and ρ_{QB} for LED_2 and LED_3 are measured and presented in Table 4. The polarization charge density at the QB_2/QW_2 interlayer with respect to the spontaneous (P_{SP}) and piezoelectric polarizations (P_{PP}) is defined [41]. The equations are as follows:

$$\sigma_{interface} = [P_{SP}(QB) - \{P_{SP}(QW) + P_{PP}(QW)\}] \times 6.242 \times 10^{18} \quad (6)$$

$$P_{SP}(\mathrm{Al_xGa_{1-x}N}) = -0.09x - 0.034(1-x) + 0.019x(1-x) \quad (7)$$

$$P_{PP}(\mathrm{Al_xGa_{1-x}N}) = \{x.P_{PP}(AlN) + (1-x).P_{PP}(AlN)\}.s \quad (8)$$

where,

$$P_{PP}(\mathrm{AlN}) = -1.808.s + 5.624.s^2 (s < 0)$$

$$P_{PP}(\mathrm{AlN}) = -1.808.s + 7.888.s^2 (s > 0)$$

$$P_{PP}(\mathrm{GaN}) = -0.918.s + 9.541.s^2$$

$$\text{Basal strain, } s = \frac{QB_{L.C} - QW_{L.C}}{QW_{L.C}}$$

The respective lattice constants (L.C) are found elsewhere [41]. The bulk charge density in the barriers, which is induced due to polarization, can be derived as shown in Equation (9) below:

$$\rho_{QB} = \frac{P_{SP}\left(\mathrm{Al_yGa_{1-y}N}\right) + P_{PP}\left(\mathrm{Al_yGa_{1-y}N}\right) - P_{SP}(\mathrm{Al_xGa_{1-x}N})}{w(y) - w(x)} \times 6.242 \times 10^{18} \quad (9)$$

where QB is graded from $\mathrm{Al_xGa_{1-x}N}$ to $\mathrm{Al_yGa_{1-y}N}$, and $|\, w(y) - w(x)|$ is the grading distance. From Table 4, $\sigma_{interface}$ is low in LED_3 compared to LED_2 because of the reduced lattice mismatch at the interfaces. However, ρ_{QB} values are high in LED_3 due to the graded configuration of the Al content. As a whole, $\Delta P(w)$ is low in LED_3 which leads to a poor electrostatic field in each QB. This, in turn, also reduces the electrostatic field in the QW. Figure 4c also predicts a lower electrostatic field in the MQW of LED_3, due to which carrier confinement is enhanced in LED_3.

Table 4. Calculated $\sigma_{interface}$ at QB/QW interface, and ρ_{QB} in the barriers of LED_2 and LED_3.

LED	$\boldsymbol{\sigma_{interface}(\times 10^{16})}$				$\boldsymbol{\rho_{QB}(\times 10^{17})}$			
	$\boldsymbol{QB_2/QW_2}$	$\boldsymbol{QB_3/QW_3}$	$\boldsymbol{QB_4/QW_4}$	$\boldsymbol{QB_5/QW_5}$	$\boldsymbol{QB_2}$	$\boldsymbol{QB_3}$	$\boldsymbol{QB_4}$	$\boldsymbol{QB_5}$
LED_2	4.789	5.876	6.983	8.112	3.535	3.565	3.599	3.636
LED_3	4.078	5.149	6.242	7.356	3.554	3.588	3.624	3.659

The IQE, LOP, current-voltage (I-V) characteristics, and electroluminescence (EL) intensity of the three LEDs are illustrated in Figure 5. The following equations establish the structure's current density (j) and it's IQE using the ABC-model.

$$\frac{j}{qd} = An + Bn^2 + Cn^3 \quad (10)$$

$$IQE = \frac{Bn}{A + Bn + Cn^2} \quad (11)$$

q = charge of electron, $A = 1/\tau$ (τ = Shockley–Read non-radiative carrier lifetime), B = radiative recombination constants, C = Auger recombination constants, d = effective width of the recombination region. The calculated maximum IQEs for LED_1, LED_2, and LED_3 are 39.3%, 47.7%, and 55.3%, respectively, as shown in Figure 5a, indicating that the effi-

ciency of LED_3 is 40.7% and 15.9% larger than that of LED_1 and LED_2, respectively. Additionally, from the inset of Figure 5a, at 60 mA injection current, the efficiency drop of LED_3 is noticeably reduced to 2.53%.

From Figure 5b, the optical power of LED_3 is remarkably increased (~17.3 mW) at a 60 mA current, which is 61.7% better compared to the conventional device. They are attributed to improved carrier transit and confinement in the MQW, greater electron and hole wave function overlap, reduced electron leakage, and improved hole injection efficiency.

As displayed in Figure 5c, all three structures have a nearly equal turn-on voltage. It is also noticeable that at a 60 mA current, LED_3 exhibits a slightly higher operating voltage because of the heart-shaped QBs and also due to the absence of EBL.

The constant analytical dependence of the anticipated IQE on the radiative current density (j_{rad}) is a further significant characteristic of the ABC model, as shown in Equation (12).

$$IQE = \frac{Q}{Q + \left(j_{rad}/j_m\right)^{\frac{1}{2}} + \left(j_{rad}/j_m\right)^{-\frac{1}{2}}} \quad (12)$$

Q = quality factor which is independent of current density and equal to $B(\tau/C)^{1/2}$ within the ABC-model. Radiative recombination rates cause the value of Q to rise while the Auger and Shockley–Read recombination rates cause it to fall. Furthermore, the magnitude of Q solely determines how dependent the IQE is on the j_{rad}/j_m ratio (j_m = qdB/τC within the ABC-model). As a result, this value may be used as a measure of merit for LED structures with varied designs, or those that emit light in diverse spectral regions.

According to Figure 6, the analytical dependence (12) accurately reproduces the IQE variation with current density in the structures of different LED designs. It is discovered that the specific value of the quality factor given in each plot correlates with both the maximum efficiency and its decline with current. This factor varies from 0.78 to 18, depending on how well each structure's design and construction materials perform overall.

For clear comparison, the calculated parameters of IQE, LOP, and efficiency drop of the three samples are summarized in Table 5.

Table 5. Optimized performance parameters for LED_1, LED_2, and LED_3.

Parameters	LED_1	LED_2	LED_3
Maximum IQE (%)	39.3 at 1.93 mA	47.7 at 3.28 mA	55.3 at 2.78 mA
IQE (%) at 60 mA	29.2	40.9	53.9
Efficiency Droop (%) at 60 mA	25.7	16.7	2.53
Luminous Power at 60 mA (mW)	10.7	13.9	17.3

Due to better radiative recombination and lower leakage of electrons, LED_3 displays dominant EL intensity at an emission wavelength of ~275 nm, as shown in Figure 5d. EL intensity of LED_3 is ~1.52 times higher than LED_1 and ~1.23 times higher than LED_2. Peak fitting is used to calculate the full width at half maximum (FWHM) of each spectrum, as illustrated in Figure 5d. The combined impacts of the larger efficient hole injection and the better capability of heart-shaped graded Al Composition in the QBs are responsible for the superiority. Strong electron confinement in the QW of LED_3 causes it to emit a relatively sharp and narrow light beam. As an outcome it has a small spectral width and FWHM. LED_1, in comparison, has substantially wider radiation patterns (beam width), which result in wider FWHM and wide spectral bands.

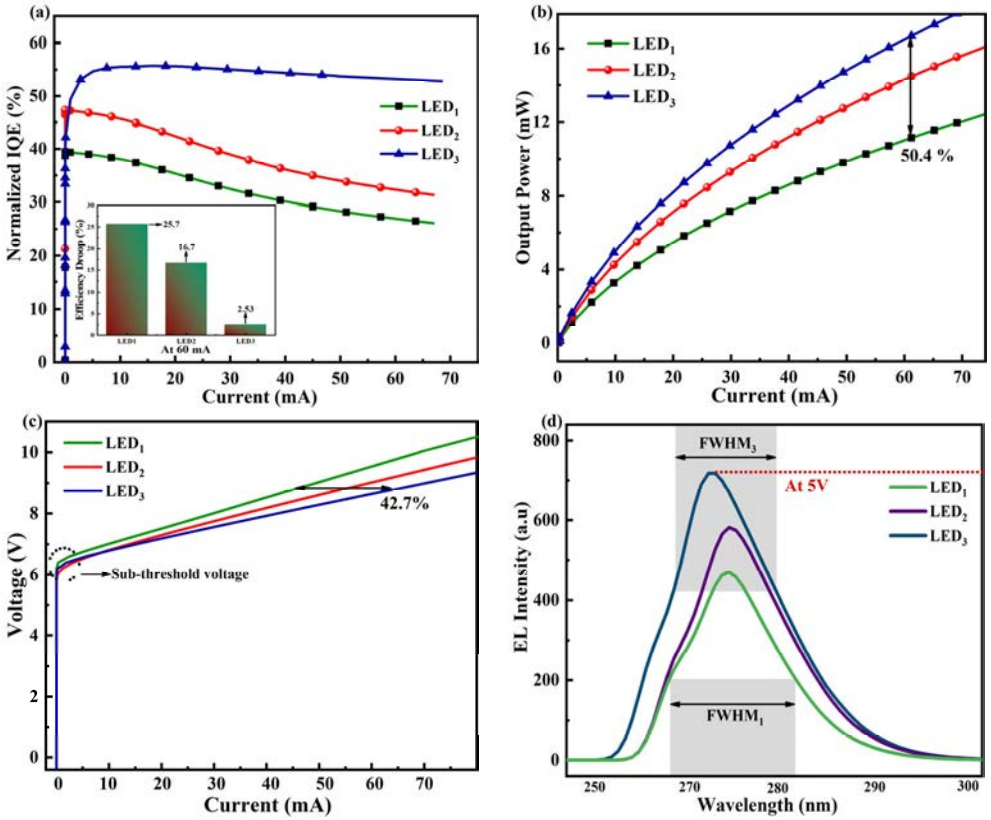

Figure 5. Measured (**a**) Efficiency, (**b**) Luminous Power, (**c**) I-V, and (**d**) EL intensity properties of LED_1, LED_2, and LED_3.

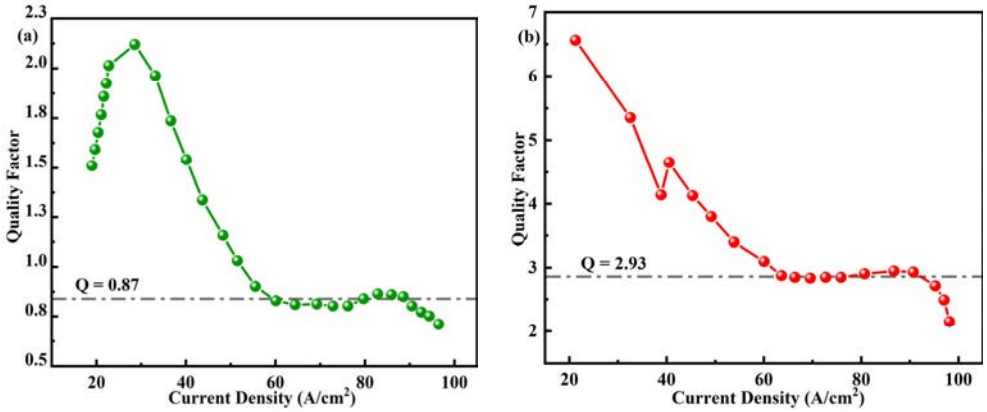

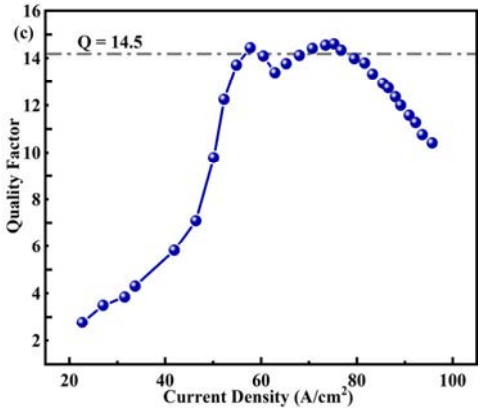

Figure 6. Quality factor as a function of current density obtained from the data reported for (**a**) LED_1, (**b**) LED_2, and (**c**) LED_3.

From Figure 7a, the optical output power of LED_3 is immensely raised along with input power supply. Also, the contrasting results of controlling the input supply in the devices is primarily ascribed to varying operational bias, as shown in Figure 5c. Figure 7b displays the wall-plug efficiency (WPE) as a factor of input current for each LED structure. The WPE of LED_3 is ~5.39% at 60 mA, which is enhanced by nearly ~49.3% compared to LED_1. The increased output power of our suggested device LED_3 is what gives it a better WPE. For better understanding, the performance parameters of our work have been compared to the recent research works and their approximate values are listed in Table 6.

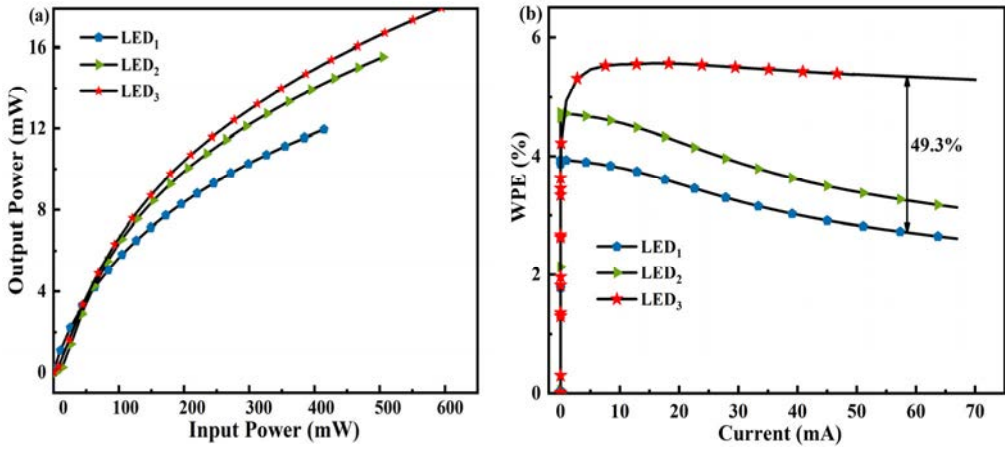

Figure 7. Approximated (**a**) output power with respect to input power, (**b**) WPE vs. injected current of LED_1, LED_2, and LED_3.

Table 6. Comparison of performance metrics with recent research works.

Author	Maximum IQE (%)	Droop (%)	Power (mW)	References
Kang et al.	27.51	3.01	8.24	[42]
Jain et al.	35.17	20.68	13.9	[43]
Velpula et al.	5.3	9.1	15.68	[44]
Ji et al.	9.16	11.24	16.11	[45]
Pandey et al.	4.12	19.21	8.91	[46]
This work	53.9	2.53	17.3	

4. Conclusions

We have explored and reported the effect of UV LEDs with heart-shaped QBs and no EBLs across a wavelength range of ~275 nm. The parameters utilized are taken from the data of the experimental reference device in order to verify the validity of the simulation results. The proposed device has an emitting layer thickness of >30 nm due to which the long-life stability is 90,000 h. These simulated results reveal that incorporating the proposed QB is advantageous for achieving high optical output power and WPE in the UV spectral range. The p-EBL free device can effectively suppress the excess flow of electrons and support a boosted hole injection. The EBL-free structure is also advantageous from the perspective of epitaxial growth because it prevents the development of p-heavy doped Al composition in the EBL. This, in turn, reduces the device resistance. The proposed structure records output power of 16.1 mW and displays increased radiative recombination, IQE of 53.9% at 60 mA which is larger than the remaining structures by 1.5 and 1.8 times, respectively. Therefore, the reported LED structure shows great potential and has the ability to produce UV LEDs with significant performances for various utilities in the practical world.

Author Contributions: S.D.: Conceptualization, Design, Simulation and Writing of manuscript; T.R.L.: Conceptualization, Supervision, Writing—review and editing and Funding; F.A.T.: Supervision, Writing—review and editing; H.P.T.N.: Supervision, Writing—review and editing; G.C.: Supervision, Writing—review and editing. All authors have read and agreed to the published version of the manuscript.

Funding: This study was funded by DST-SERB: Government of India sponsored MATRICS Project No. MTR/2021/000370 and US National Science Foundation, under grant number 1944312.

Data Availability Statement: The data and materials may be available on request basis.

Acknowledgments: This work is the outcome of DST-SERB, Govt. of India sponsored MATRICS Project No. MTR/2021/000370 which is duly acknowledged for kind support. H. P. T. Nguyen also acknowledges financial support from the US National Science Foundation, under grant number 1944312.

Conflicts of Interest: The authors declare no conflicts of interest.

References

1. Muramoto, Y.; Kimura, M.; Nouda, S. Development and future of ultraviolet light-emitting diodes: UV-LED will replace the UV lamp. *Semicond. Sci. Technol.* **2014**, *29*, 084004. https://doi.org/10.1088/0268-1242/29/8/084004.
2. Gassie, L.W.; Englehardt, J.D. Advanced oxidation and disinfection processes for onsite net-zero greywater reuse: A review. *Water Res.* **2017**, *125*, 384–399. https://doi.org/10.1016/j.watres.2017.08.062.
3. Zhou, X.; Li, Z.; Lan, J.; Yan, Y.; Zhu, N. Kinetics of inactivation and photoreactivation of Escherichia coli using ultrasound-enhanced UV-C light-emitting diodes disinfection. *Ultrason. Sonochem.* **2017**, *35*, 471–477. https://doi.org/10.1016/j.ultsonch.2016.10.028.
4. Rattanakul, S.; Oguma, K. Analysis of Hydroxyl Radicals and Inactivation Mechanisms of Bacteriophage MS_2 in Response to a Simultaneous Application of UV and Chlorine. *Environ. Sci. Technol.* **2017**, *51*, 455–462. https://doi.org/10.1021/acs.est.6b03394.
5. Rattanakul, S.; Oguma, K. Inactivation kinetics and efficiencies of UV-LEDs against Pseudomonas aeruginosa, Legionella pneumophila, and surrogate microorganisms. *Water Res.* **2018**, *130*, 31–37. https://doi.org/10.1016/j.watres.2017.11.047.
6. Okamura, H.; Niizeki, S.; Ochi, T.; Matsumoto, A. UV curable formulations for UV-C LEDs. *J. Photopolym. Sci. Technol.* **2016**, *29*, 99–104. https://doi.org/10.2494/photopolymer.29.99.
7. Okamura, H.; Matoba, T.; Takada, K.; Yamashita, M.; Shirai, M.; Matsumoto, A. Photo-thermal dual curing of acrylic anchor resins for screen printing. *Prog. Org. Coat.* **2016**, *100*, 47–50. https://doi.org/10.1016/j.porgcoat.2016.01.025.
8. Yamazaki, S.; Nishioka, A.; Kasuya, S.; Ohkura, N.; Hemmi, H.; Kaisho, T.; Taguchi, O.; Sakaguchi, S.; Morita, A. Homeostasis of Thymus-Derived $Foxp3^+$ Regulatory T Cells Is Controlled by Ultraviolet B Exposure in the Skin. *J. Immunol.* **2014**, *193*, 5488–5497. https://doi.org/10.4049/jimmunol.1400985.
9. Nakamura, M.; Morita, A.; Seité, S.; Haarmann-Stemmann, T.; Grether-Beck, S.; Krutmann, J. Environment-induced lentigines: Formation of solar lentigines beyond ultraviolet radiation. *Exp. Dermatol.* **2015**, *24*, 407–411. https://doi.org/10.1111/exd.12690.
10. Fujishima, A.; Zhang, X. Titanium dioxide photocatalysis: Present situation and future approaches. *Comptes Rendus Chim.* **2006**, *9*, 750–760. https://doi.org/10.1016/j.crci.2005.02.055.

11. Nakata, K.; Fujishima, A. TiO_2 photocatalysis: Design and applications. *J. Photochem. Photobiol. C Photochem. Rev.* **2012**, *13*, 169–189. https://doi.org/10.1016/j.jphotochemrev.2012.06.001.
12. Das, S.; Lenka, T.R.; Talukdar, F.A.; Velpula, R.T.; Jain, B.; Nguyen, H.P.T.; Crupi, G. Effects of polarized-induced doping and graded composition in an advanced multiple quantum well InGaN/GaN UV-LED for enhanced light technology. *Eng. Res. Express* **2022**, *4*, 015030. https://doi.org/10.1088/2631-8695/ac4fb1.
13. Khan, M.A.; Shatalov, M.; Maruska, H.P.; Wang, H.M.; Kuokstis, E. III-nitride UV devices. *Jpn. J. Appl. Phys.* **2005**, *44*, 7191–7206. https://doi.org/10.1143/JJAP.44.7191.
14. Uhlin, F.; Fridolin, I.; Lindberg, L.G.; Magnusson, M. Estimating total urea removal and protein catabolic rate by monitoring UV absorbance in spent dialysate. *Nephrol. Dial. Transplant.* **2005**, *20*, 2458–2464. https://doi.org/10.1093/ndt/gfi026.
15. Tomson, R.; Uhlin, F.; Fridolin, I. Urea rebound assessment based on UV absorbance in spent dialysate. *ASAIO J.* **2014**, *60*, 459–465. https://doi.org/10.1097/MAT.0000000000000091.
16. Cho, J.; Schubert, E.F.; Kim, J.K. Efficiency droop in light-emitting diodes: Challenges and counter measures. *Laser Photonics Rev.* **2013**, *7*, 408–421. https://doi.org/10.1002/lpor.201200025.
17. Pieniak, K.; Chlipala, M.; Turski, H.; Trzeciakowski, W.; Muziol, G.; Staszczak, G.; Kafar, A.; Makarowa, I.; Grzanka, E.; Grzanka, S.; et al. Quantum-confined Stark effect and mechanisms of its screening in InGaN/GaN light-emitting diodes with a tunnel junction. *Opt. Express* **2021**, *29*, 1824. https://doi.org/10.1364/oe.415258.
18. Hirayama, H.; Fujikawa, S.; Noguchi, N.; Norimatsu, J.; Takano, T.; Tsubaki, K.; Kamata, N. 222–282 nm AlGaN and InAlGaN-based deep-UV LEDs fabricated on high-quality AlN on sapphire. *Phys. Status Solidi* **2009**, *206*, 1176–1182. https://doi.org/10.1002/pssa.200880961.
19. Chu, C.; Tian, K.; Che, J.; Shao, H.; Kou, J.; Zhang, Y.; Li, Y.; Wang, M.; Zhu, Y.; Zhang, Z.-H. On the origin of enhanced hole injection for AlGaN-based deep ultraviolet light-emitting diodes with AlN insertion layer in p-electron blocking layer. *Opt. Express* **2019**, *27*, A620. https://doi.org/10.1364/oe.27.00a620.
20. Velpula, R.T.; Jain, B.; Bui, H.Q.T.; Shakiba, F.M.; Jude, J.; Tumuna, M.; Nguyen, H.-D.; Lenka, T.R.; Nguyen, H.P.T. Improving carrier transport in AlGaN deep-ultraviolet light-emitting diodes using a strip-in-a-barrier structure. *Appl. Opt.* **2020**, *59*, 5276. https://doi.org/10.1364/ao.394149.
21. Nakarmi, M.L.; Nepal, N.; Lin, J.Y.; Jiang, H.X. Photoluminescence studies of impurity transitions in Mg-doped AlGaN alloys. *Appl. Phys. Lett.* **2009**, *94*, 10–13. https://doi.org/10.1063/1.3094754.
22. Nam, K.B.; Nakarmi, M.L.; Li, J.; Lin, J.Y.; Jiang, H.X. Mg acceptor level in AlN probed by deep ultraviolet photoluminescence. *Appl. Phys. Lett.* **2003**, *83*, 878–880. https://doi.org/10.1063/1.1594833.
23. Zhang, Z.H.; Chen, S.-W.H.; Chu, C.; Tian, K.; Fang, M.; Zhang, Y.; Bi, W.; Kuo, H.-C. Nearly efficiency-droop-free algan-based ultraviolet light-emitting diodes with a specifically designed superlattice P-type electron blocking layer for high MG doping efficiency. *Nanoscale Res. Lett.* **2018**, *13*, 122. https://doi.org/10.1186/s11671-018-2539-9.
24. Das, S.; Lenka, T.R.; Talukdar, F.A.; Velpula, R.T.; Nguyen, H.P.T. Efficiency and Radiative Recombination Rate Enhancement in GaN/AlGaN Multi-Quantum Well-Based Electron Blocking Layer Free UV-LED for Improved Luminescence. *FACTA Univ. Ser. Electron. Energ.* **2023**, *36*, 91–101. https://doi.org/10.2298/FUEE2301091D.
25. Das, S.; Lenka, T.R.; Talukdar, F.A.; Sadaf, S.M.; Velpula, R.T.; Nguyen, H.P.T. Impact of a prestrained graded InGaN/GaN interlayer towards enhanced optical characteristics of a multi-quantum well LED based on silicon substrate. *Appl. Opt.* **2022**, *61*, 8951–8958. https://doi.org/10.1364/AO.470083.
26. Philip, M.R.; Choudhary, D.D.; Djavid, M.; Le, K.Q.; Piao, J.; Nguyen, H.P.T. High efficiency green/yellow and red InGaN/AlGaN nanowire light-emitting diodes grown by molecular beam epitaxy. *J. Sci. Adv. Mater. Devices* **2017**, *2*, 150–155. https://doi.org/10.1016/j.jsamd.2017.05.009.
27. Liu, C.; Melanson, B.; Zhang, J. Algan-delta-gan quantum well for duvleds. *Photonics* **2020**, *7*, 87. https://doi.org/10.3390/photonics7040087.
28. Das, S.; Lenka, T.R.; Talukdar, F.A.; Nguyen, H.P.T.; Crupi, G. The role of indium composition in InxGa1-xN prestrained layer towards optical characteristics of EBL free GaN/InGaN nanowire LEDs for enhanced luminescence. *Int. J. Numer. Model.* **2023**, *36*, e3169. https://doi.org/10.1002/jnm.3169.
29. Varshni, Y.P. Temperature dependence of the energy gap in semiconductors. *Physica* **1967**, *34*, 149–154.
30. Piprek, J. *Nitride Semiconductor Devices: Principles and Simulation*; Wiley Online Library: Berlin, Germany, 2007; Volume 590.
31. Nunez-Gonzalez, R. First-principles calculation of the band gap of $Al_xGa_{1-x}N$ and $In_xGa_{1-x}N$. *Rev. Mex. Fis.* **2008**, *54*, 111–118.
32. Chuang, S.; Chang, C. K · p method for strained wurtzite semiconductors. *Phys. Rev. B* **1996**, *54*, 2491–2504. https://doi.org/10.1103/PhysRevB.54.2491.
33. Caughey, D.M.; Thomas, R.E. Carrier Mobilities in Silicon Empirically Related to Doping and Field. *Proc. IEEE* **1967**, *55*, 2192–2193. https://doi.org/10.1109/PROC.1967.6123.
34. Yun, J.; Shim, J.I.; Hirayama, H. Analysis of efficiency droop in 280-nm AlGaN multiple-quantum-well light-emitting diodes based on carrier rate equation. *Appl. Phys. Express* **2015**, *8*, 022104. https://doi.org/10.7567/APEX.8.022104.
35. Hirayama, H. Recent Progress in AlGaN Deep-UV LEDs. In *Light-Emitting Diode: An Outlook On the Empirical Features and Its Recent Technological Advancements*; BoD—Books on Demand: London, UK, 2018; https://doi.org/10.5772/intechopen.79936.
36. Fiorentini, V.; Bernardini, F.; Ambacher, O. Evidence for nonlinear macroscopic polarization in III-V nitride alloy heterostructures. *Appl. Phys. Lett.* **2002**, *80*, 1204–1206. https://doi.org/10.1063/1.1448668.

37. Vurgaftman, I.; Meyer, J.R. Band parameters for nitrogen-containing semiconductors. *J. Appl. Phys.* **2003**, *94*, 3675–3696. https://doi.org/10.1063/1.1600519.
38. Das, S.; Lenka, T.R.; Talukdar, F.A.; Velpula, R.T.; Nguyen, H.P.T. Design and analysis of novel high-performance III-nitride MQW-based nanowire white-LED using HfO_2/SiO_2 encapsulation. *Opt. Quantum Electron*. **2023**, *55*, 67. https://doi.org/10.1007/s11082-022-04350-y.
39. Xu, Q.; Niu, Y.; Li, J.; Yang, Z.; Gao, J.; Ding, L.; Ni, H.; Zhu, P.; Liu, Y.; Tang, Y.; et al. Recent progress of quantum dots for energy storage applications. *Carbon Neutrality* **2022**, *1*, 13. https://doi.org/10.1007/s43979-022-00002-y.
40. Zhang, Z.H.; Liu, W.; Ju, Z.; Tan, S.T.; Ji, Y.; Kyaw, Z.; Zhang, X.; Wang, L.; Sun, X.W.; Demir, H.V. Self-screening of the quantum confined Stark effect by the polarization induced bulk charges in the quantum barriers. *Appl. Phys. Lett.* **2014**, *104*, 16–21. https://doi.org/10.1063/1.4883894.
41. Ambacher, O.; Dimitrov, R.; Stutzmann, M.; Foutz, B.E.; Murphy, M.J.; Smart, J.A.; Shealy, J.R.; Weimann, N.G.; Chu, K.; Chumbes, M.; et al. Role of spontaneous and piezoelectric polarization induced effects in group-III nitride based heterostructures and devices. *Phys. Status Solidi Basic Res.* **1999**, *216*, 381–389. https://doi.org/10.1002/(SICI)1521-3951(199911)216:1<381::AID-PSSB381>3.0.CO;2-O.
42. Kang, Y.; Yu, H.; Ren, Z.; Xing, C.; Liu, Z.; Jia, H.; Guo, W.; Sun, H. Efficiency Droop Suppression and Light Output Power Enhancement of Deep Ultraviolet Light-Emitting Diode by Incorporating Inverted-V-Shaped Quantum Barriers. *IEEE Trans. Electron. Devices* **2020**, *67*, 4958–4962. https://doi.org/10.1109/TED.2020.3025523.
43. Jain, B.; Velpula, R.T.; Patel, M.; Sadaf, S.M.; Nguyen, H.P.T. Improved performance of electron blocking layer free algan deep ultraviolet light-emitting diodes using graded staircase barriers. *Micromachines* **2021**, *12*, 334. https://doi.org/10.3390/mi12030334.
44. Jain, B.; Velpula, R.T.; Velpula, S.; Nguyen, H.-D.; Nguyen, H.P.T. Enhanced hole transport in AlGaN deep ultraviolet light-emitting diodes using a double-sided step graded superlattice electron blocking layer. *J. Opt. Soc. Am. B* **2020**, *37*, 2564. https://doi.org/10.1364/josab.399773.
45. Ji, Y.; Zhang, Z.H.; Kyaw, Z.; Tan, S.T.; Ju, Z.G.; Zhang, X.L.; Liu, W.; Sun, X.W.; VolkanDemir, H. Influence of n-type versus p-type AlGaN electron-blocking layer on InGaN/GaN multiple quantum wells light-emitting diodes. *Appl. Phys. Lett*. **2013**, *103*, 053512. https://doi.org/10.1063/1.4817381.
46. Pandey, A.; Shin, W.J.; Liu, X.; Mi, Z. Effect of electron blocking layer on the efficiency of AlGaN mid-ultraviolet light emitting diodes. *Opt. Express* **2019**, *27*, A738. https://doi.org/10.1364/oe.27.00a738.